ARTICLE   OPEN

Check for updates

Giant linear magnetoresistance in half-metallic Sr$_2$CrMoO$_6$ thin films

Zhao-Cai Wang[1], Lei Chen[2], Shuang-Shuang Li[1], Jing-Shi Ying[1], F. Tang[3], Guan-Yin Gao [4], Y. Fang[3], Weiyao Zhao [2,5✉], David Cortie[2,5], Xiaolin Wang[2,5] and Ren-Kui Zheng [1✉]

Linear magnetoresistance (LMR) is a special case of a magnetic-field induced resistivity response, which has been reported in highly disordered semiconductor systems and in topological materials. In this work, we observe LMR effect in half-metallic perovskite Sr$_2$CrMoO$_6$ thin films, of which the maximum MR value exceeds +1600% at 2 K and 14 T. It is an unusual behavior in ferrimagnetic double perovskite material like Sr$_2$CrMoO$_6$, which are known for intrinsic tunneling-type negative magnetoresistance. In the thin films, the high carriers' density (~10^{22} cm^{-3}) and ultrahigh mobility (~10^4 cm^2 V^{-1} s^{-1}) provide a low-resistivity (~10 nΩ·cm) platform for spin-polarized current. Our DFT calculations and magnetic measurements further support the half-metal band structure. The LMR effect in Sr$_2$CrMoO$_6$ could possibly originate from transport behavior that is governed by the guiding center motion of cyclotron orbitals, where the magnetic domain structure possibly provides disordered potential. The ultrahigh mobility and LMR in this system could broaden the applications of perovskites, and introduce more research on metallic oxide ferri-/ferro-magnetic materials.

INTRODUCTION

Magnetoresistance (MR) is the responding of resistance of a conductor to external magnetic field, which describes the charge carriers' scattering mechanism. In a typical metal with closed Fermi surface, the MR is parabolic-like in low magnetic field region and turns to saturation (usually several or tens of percent) in strong field limits, which, in contrast, never saturates to metal with open Fermi surfaces. Special cases appear in compensated semimetals like Bismuth or compounds like WTe$_2$[1] and NbSb$_2$[2,3] which possess both electron and hole pockets at Fermi surface, and the carrier densities are of similar value, giving rise to a giant parabolic-like MR that is always present (reaching millions of percent at ~10T), without a sign of saturation even at 60 T field. Another important MR behavior shows linear magnetic-field-dependence of resistance with no saturation (LMR), which has been found in highly disordered system such as InSb[4], Ag$_{2-\delta}$X (X = Se, Te)[4–6], topological insulators, Bi$_2$Te$_3$ family[7], Dirac or Weyl semimetals TlBiSSe[8], TaAs[9], Na$_3$Bi[10], Cd$_2$As$_3$[11,12]. Recently, LMR has also been reported in perovskite material SrRuO$_3$ thin films, which is a ferromagnetic Weyl semimetal[13]. Although the phenomenon of LMR is quite straightforward, the mechanism or explanation is complicated and has attracted increasing study in the past decade.

To further discuss the LMR effect, we should revisit some general ideas about MR. In a condensed Fermi gas system with approximately spherical Fermi surface system, the electrons travel in straight lines between collisions, and the resistivity obeys the famous formula: $\rho_0 = m^*/ne^2\tau$, in which e is the charge of an electron, n is the electron's density, m^* is the effective mass, and τ is the relaxation time. With an applied magnetic field B, the Lorentz force $e\mathbf{v} \times \mathbf{B}$ bends the path of electrons, resulting in an additional angular velocity $\omega_c = eB/m^*$. It means that the angle turned between collisions is $\omega_c\tau = B\sigma_0/ne$, and unless $\omega_c\tau > 1$, no obvious MR effect is expected. With a large enough magnetic field applied ($\omega_c\tau \gg 1$), the electron trajectories can be described in the combination of fast cyclotron orbit motion $\mathbf{r}(t)$, and slow guiding-center (GC) motion $\mathbf{R}(t)$. The cyclotron motion $\mathbf{r}(t)$ with the characteristic radius r_c, depends on materials' fermiology and B, whereas the GC motion $\mathbf{R}(t)$ depends on the potential of the electron over one cycle[14]. In a material with slowly varying disorder potentials (the potential disorder correlation length $\xi \gg r_c$), electron trajectories are dominated by the GC motion, which follows the local disorder landscape. In this case, MR is dominated by the GC motion and shows linear dependence on the magnetic field above the turn-on magnetic field[7].

In metals with long-range ferro-/ferri-magnetic ordering, intrinsic tunneling-type negative magnetoresistance (TMR) is usually observed, e.g., in Fe$_3$O$_4$[15], Tl$_2$Mn$_2$O$_7$[16], and La$_{2/3}$Sr$_{1/3}$MnO$_3$[17]. Similarly, the double perovskite A$_2$BB'O$_6$ family (A = Ca, Sr, and Ba; B = Cr, Mn, Fe, Co, and Ni, B' = Mo, W, Re, Ru, Os, Rh, Ir) is also famous for offering high magnetic ordering temperatures (>400 K) and large negative MR values[18–24], e.g., Sr$_2$FeMoO$_6$ is known for its room-temperature TMR of ~−10%[19]. In this work, we observe unconventional positive LMR effect in epitaxial Sr$_2$CrMoO$_6$ (SCMO) thin films on SrTiO$_3$ (STO) substrates at low temperatures, which may attract further study of double perovskite of this family. The positive LMR is usually related to high mobility Dirac materials, and attracts wide transport, photoemission, and scanning tunneling microscopy/spectrum studies. We propose that the LMR effect in SCMO may originate from the GC motion dominant transport, where the magnetic domain structures provide the slow-varying disordered potential.

[1]School of Materials Science and Engineering and Jiangxi Engineering Laboratory for Advanced Functional Thin Films, Nanchang University, Nanchang, China. [2]Institute for Superconducting and Electronic Materials, Innovation Campus, University of Wollongong, Wollongong, NSW, Australia. [3]Jiangsu Laboratory of Advanced Functional Materials, Department of Physics, Changshu Institute of Technology, Changshu, China. [4]Hefei National Laboratory for Physical Sciences at the Microscale, University of Science and Technology of China, Hefei, China. [5]ARC Centre of Excellence in Future Low-Energy Electronics Technologies FLEET, University of Wollongong, Wollongong, NSW, Australia. ✉email: wz929@uowmail.edu.au; zrk@ustc.edu
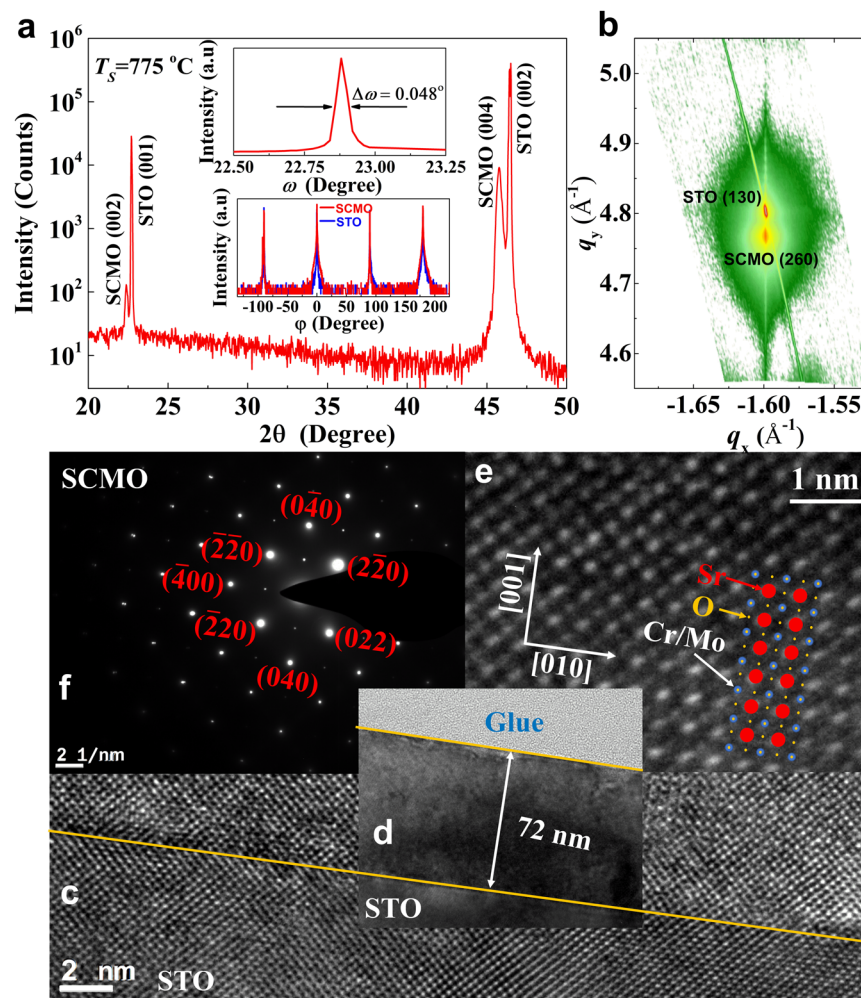
Fig. 1 Crystallographic structure of the SCMO thin film. a XRD patterns of SCMO thin film on STO substrate, sample S_5. The upper and lower insets demonstrate the rocking curve taken around (004) peak of SCMO and the XRD φ-scan patterns for the film (red curve) and substrate (blue curve), respectively. **b** X-ray reciprocal space mapping of S_5 in a certain q range, in which, the relatively smaller peak with stronger intensity is STO's (130) peak. **c–f** HRTEM images of sample S_5: panel (**d**) demonstrates that the SCMO thin film thickness is ~72 nm, with an atomically smooth surface and interface indicated by the yellow line. Panel **c** and **e** show the atomically resolved images near STO-SCMO boundary, which witnesses the nearly perfect crystallization of SCMO thin film. The SAED pattern of SCMO thin film is displayed in panel **f**, in which we indexed several bright points based on $F_{m\bar{3}m}$ space group.

RESULTS AND DISCUSSION

Structural properties

Since the electronic transport properties of thin films are highly dependent on the crystallization quality of thin films, we conducted a series of measurements to demonstrate the excellent quality of SCMO thin films. The deposition condition was already optimized in the previous steps, leaving the deposition time as the only variable in the thin-film samples, which are: S_1, 2.5 min, ~6 nm; S_2, 5 min, ~12 nm; S_3, 10 min, ~24 nm; S_4, 20 min, ~48 nm; S_5 30 min, ~72 nm; S_6, 45 min, ~108 nm; and S_7, 90 min ~216 nm. As an example, the crystallization quality of S_5 characterizations through X-ray based technique and HRTEM are shown in Fig. 1a–f. In the XRD $\theta-2\theta$ scan, the sharp cubic SCMO (004) peak locates on the shoulder of the STO (002) peak (Fig. 1a), the full width at half-maximum (FWHM) value of which is only 0.048° according to the rocking curve scan, as shown in the upper inset of Fig. 1a, which suggests high crystalline quality of this sample. The sharp diffraction peaks of other samples are shown in Supplementary Fig. S1a. The FWHM values of all samples are within 0.09°, which decreases with the increase of deposition time (in below 45 min regime), suggesting the increasing thin film crystallization quality in thicker samples within 108 nm region, as demonstrated in Fig. S1c. XRD phi scan

patterns, as shown in the lower inset of Fig. 1a, show that the SCMO film grows epitaxially on the STO substrate. Further, the XRD intensity reciprocal space mapping is plotted in Fig. 1b in the $-1.7\,\text{Å}^{-1} < q_x < -1.5\,\text{Å}^{-1}$, and $4.55\,\text{Å}^{-1} < q_y < 5.05\,\text{Å}^{-1}$ regions, in which one can observe two peaks indexed by STO (130) and SCMO (260). The sharp SCMO XRD peak suggests the nearly perfect atomic layout in our sample. The XRD results of all samples are listed in Supplementary Fig. S1, in which one may notice that the SCMO (004) peaks' positions shift to higher angle in thinner samples, suggesting the strain effect in those thin films. To study the strain effect, we carefully fitted the diffraction patterns near $2\theta = 46\,°$ with two Gaussian peaks. The obtained peak positions are summarized in Fig. S1c, in which one can see the SCMO (004) peaks are at the same position in 48–216 nm thin films. Therefore, we argue that the transport behavior in thin films above 48 nm thickness are less affected by the interfacial strain effect. We further zoom-in to the atomic view employing the HRTEM equipment, shown in Fig. 1c–f. In the low-resolution image (Fig. 1d), the thin film is sandwiched by STO substrate and amorphous glue, the interfaces of which are atomically smooth (Fig. 1c), indicated by the yellow lines. The high-resolution images near the substrate cross-section are shown in Fig. 1c, in which the coherent STO-SCMO
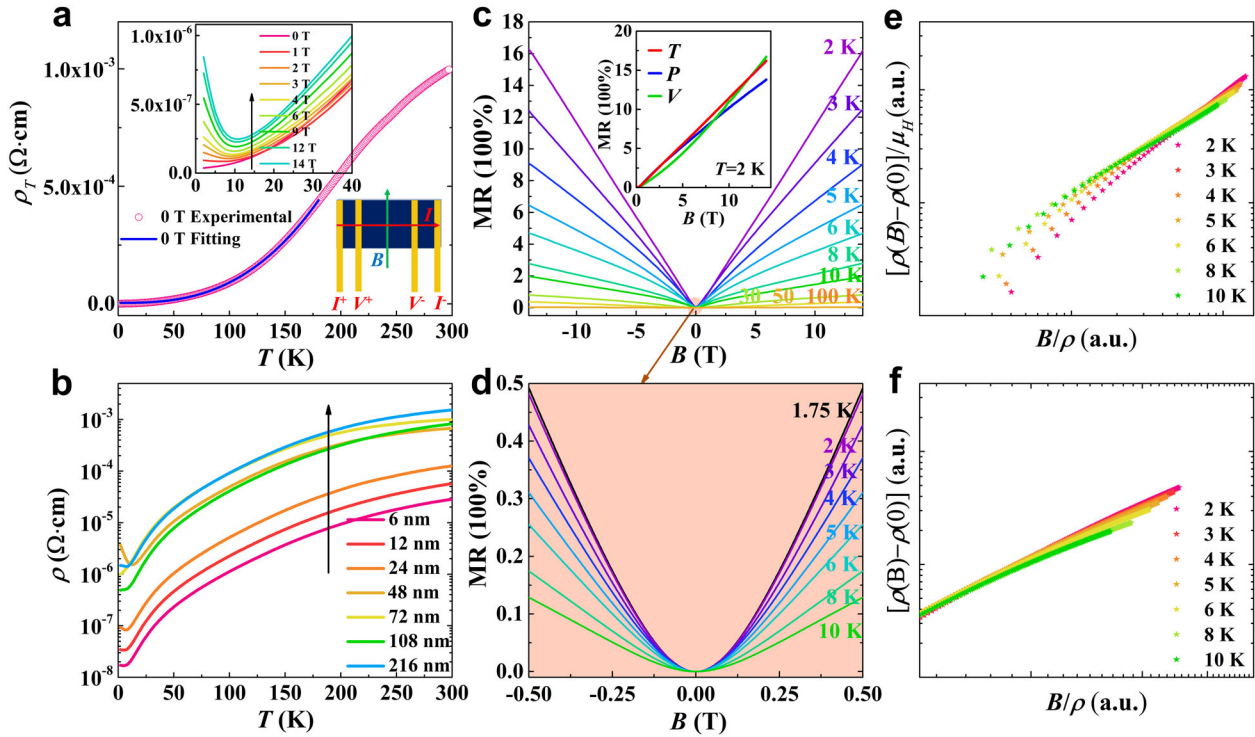
Fig. 2 **Transport properties of SCMO thin films.** **a** Temperature-dependent resistivity curve of S_5 sample from 2 to 300 K in the absence of a magnetic field. Inset: the RT curves from 2 to 40 K at various magnetic fields up to 14 T. **b** The zero-field RT curves from 2 to 300 K of SCMO thin films: S_1–S_7. **c** The MR curves of S_5 sample at various temperatures from 2 to 100 K, the low-field zoomed-in measurements are plotted in panel **d**. Inset: the MR curve in different configurations at 2 K. **e**, **f** The Kohler's plots of MR curves in panel **c**, **d**, respectively, in which the scaling rules are slightly different.

interface is evidence of the high quality of epitaxial thin film of our sample. Since the cubic SCMO possesses a lattice constant of 7.865 Å which is slightly larger than two of STO lattice constants (2 × 3.905 Å = 7.810 Å), one can see lattice compressive distortion, which tends to relax quickly. Since the XRD and HRTEM provide evidence that the strained layers are negligible, they would not dominant the total transport or magnetic properties in our sample set. A zoomed-in bright field image of the SCMO atomic structure is shown in Fig. 1e, in which we superimposed three SCMO unit cells along (001) direction, to show the stacking of the atoms. The selected area electron diffraction (SAED) pattern of SCMO sample is demonstrated in Fig. 1f, in which the sharpest spots are indexed in $F_{m\bar{3}m}$ space group. The XRD and HRTEM results demonstrate the excellent quality of the epitaxial SCMO thin films, supporting the further magnetic and transport measurements. Another evidence of the film quality is the nano-/sub-nano magnitude of surface mean square roughness, which is shown in Supplementary Fig. S2 and Supplementary Table S1.

Electronic transport properties

The temperature and magnetic field-dependent resistivity curves were measured by four-parallel electrodes configuration, as sketched in the inset of Fig. 2a, where the applied *transverse* magnetic fields are in the thin-film plane, and perpendicular to the current (T configuration). Another two measurement configurations were also applied to measure all samples, which are: the in-plane magnetic field *parallel* to the current (P configuration), and the out-of-plane *vertical* magnetic field parallel to the normal vector of the thin film (V configuration). At zero field, the temperature-dependent resistivity (T) of S_5 behaves as a good metal, with 2K = 52 nΩ·cm and 300K = 65.9 μΩ·cm, as shown in Fig. 2a. The resistivity is comparable to half-metallic Sr₂CrWO₆, e.g., 2K = 4.9–92 nΩ·cm and 300K = 95–370 μΩ·cm for 12–48 nm thin

films on STO substrates, as well as the residual resistivity ratio (RRR), i.e., $RRR(S_5)$ = 1267, and RRR(Sr₂CrWO₆) = 2444–19,387[25]. The zero-field T curve below 175 K can be quite well fitted using the equation $\rho(T) = \rho_0 + AT^n$ (Fig. 2a), where ρ_0 is the residual resistivity, A is a constant, and n is the parameter indicating scattering mechanisms. The obtained residual resistivity ρ_0 = 20 nΩ·cm, and n = 2.7 is close to that of the topological semimetal single crystals, e.g., $n \sim 3$ for Cd₃As₂[26] and ZrSiS family[27,28]. This type of temperature dependence of resistivity, deviating from the pure electronic correlation-dominated scattering mechanism (n = 2), can be attributed to the interband electron-phonon scattering[28]. In Fig. 2b, for thinner films (6–24 nm), the resistivity increases with film thickness, however, the thickness dependent behavior vanishes for 48–216 nm thin films. Based on the XRD pattern fittings, one can see that for the 6–24 nm thin films, the interfacial strain effect is more pronounced. Therefore, we deduce that the carriers' density (Fig. 3a) and conductivity are positively related to the interfacial strain. For thin films with thickness above 48 nm, the interfacial strain is relaxed, and the resistivity show less thickness dependence.

The Hall effect was measured for S_1–S_7, to characterize the carrier properties of the SCMO samples. The total Hall effect shows linear-like decreasing curves, which corresponds to an n-type conductor contributing electron carriers, as shown in Fig. S13. From the Hall effect curves, we can calculate the Hall coefficient R_H, and thus obtain the carrier density via $n_H = 1/R_H e$ (e is the charge of an electron) and Hall mobility $\mu_H = \sigma R_H$ (σ is the conductivity), which are shown in Fig. 3a, b. The carrier density n_H of all samples are in 10^{21}–10^{22} cm^{-3} range, and for each sample, n_H increases monotonically during heating. Due to the half-metallic band structure, which will be further discussed below, the carriers in SCMO are fully spin polarized. The combination of fully spin polarization, high n_H and high μ_H is rare in metallic materials, which paves an avenue to low-dissipation spintronic devices.
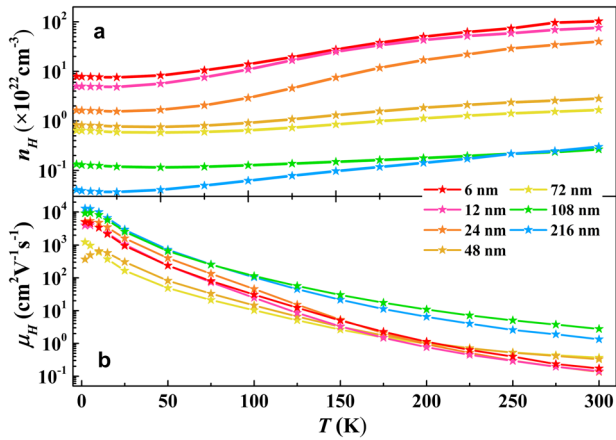
Fig. 3 The Carrier properties of SCMO thin films S_1–S_5. a carrier density, and **b** Hall mobility.

Table 1. The carrier characterization of samples S_1–S_7 at 2 K.

	S_1	S_2	S_3	S_4	S_5	S_6	S_7
n_H (10^{22} cm^{-3})	7.9	5.0	2.0	0.83	0.63	0.13	0.04
μ_H (cm^2 V^{-1} s^{-1})	4910	3913	5020	366	1225	9115	12755
l_e (μm)	17.6	15.8	18.1	1.2	4.3	17.8	19.5

Unlike a typical metal, the carriers' mobility is much higher at low temperatures (10^3–10^4 cm^2/Vs), which decreases with heating dramatically. One can estimate the mean free path $l_e = \frac{\hbar\sqrt{2\pi n}}{e}\mu$, where $n = n_H$ is the carrier's area density, $\mu = \mu_H$ is the carrier's mobility, e is the charge of electron, e.g., l_e ($S_{5\_2\,K}$) = 4.3 μm. The carrier density, Hall mobility and mean free path for S_1–S_7 at 2 K are listed in Table 1.

With *transverse* applied magnetic fields, the resistivity shows an upturn below 10 K as shown in the inset of Fig. 2a, which is similar to topological semimetals. There are several models related to magnetic induced resistivity upturn effect, e.g., Tafti et al.[29] attributed the upturn in LaSb single crystal to magnetic-field-induced gap opening, on the contrary, Jo et al.[30] provided enough evidence to verify the absence of gap opening during the upturn and simply employed Kohler's scaling rule to explain this phenomenon in PtSn$_4$. In order to further investigate this upturn effect, we conducted magnetic field-dependent resistivity (MR) measurements at various temperatures on S_5, with a *transverse* magnetic field. As shown in Fig. 2b, the samples with different thicknesses show roughly similar zero-field RT behavior with S_5, which only varies in resistivity values, (with applied magnetic fields, the resistivity upturn effect is universal in SCMO system, as shown in Supplementary Figs. S3–S9).

As shown in Fig. 2c, the (*T* configuration) MR values of S_5 from 2 K to 100 K, up to 14 T, are in the positive region, unlike those tunneling-type negative MR in Sr$_2$FeMoO$_6$[19] and related double perovskites. In the present scale magnitude, one may notice that the MR curve at 2 K from 0 to ±14 T shows linearly increasing with the magnetic field, with no sign of saturation, and reached more than 1600% at ±14 T. The 14-T-MR value decreases dramatically during heating, which is ~ 1230% at 3 K, ~900% at 4 K, and only 200% at 10 K. As shown in Supplementary Fig. S11, the 14-T-MR values can be roughly fitted in an inverse proportional function, which is quite different from the behavior in topological semimetals, e.g., 14-T-MR of ZrGeSe are nearly constant below ~20 K region[27]. Another inversely-proportional feature can be found in the Hall mobility μ_H, which is also demonstrated in Supplementary Fig. S11. In topological semimetals, the low-temperature resistivity form plateaus without and with magnetic fields[1–3,27,28], where the

resistivity values only change with the magnetic fields. However in SCMO, the resistivity changes with the temperature significantly, similar to the situation in Sr$_2$CrWO$_6$[25]. With further heating, the MR values decrease monotonically, reaching only a few percent at 100 K. The LMR was also observed in other measuring configurations, either with parallel magnetic fields (*P* configuration), or vertical magnetic fields (*V* configuration), as shown in Supplementary Fig. S7, in which the main features are consistent: (1) linear, or quasi-linear field-dependent behavior is dominant in high fields and low temperatures; (2) MR values at 14 T decreases fast with heating due to the mobility cascading, which are neglectable at ~ 100 K. The MR behavior among configurations are slightly different, e.g., 1620, 1380 and 1670% for *T*, *P* and *V* configurations (at 2 K and 14 T) respectively.

As abovementioned, the LMR is quite rare in solids, only observed in inhomogeneous systems, or in some high mobility topological materials. Since the XRD results and HRTEM images demonstrate the high quality of thin films, and there is no evidence relating the band structure to topology, the origin of this surprising LMR effect in SCMO may trigger everyone's curiosity. First of all, one may notice that the thin films were deposited in high temperature and high vacuum condition, which induces oxygen vacancies in both SCMO films and STO substrates. Owing to the intrinsic metallic nature of SCMO, and intrinsic insulating nature to STO, oxygen vacancies behave differently in thin film and substrate. With increasing oxygen vacancy level, the defect scattering of electrons becomes significant, which can even tune the transport behavior to semiconducting in some perovskites[25]. Therefore, the high conductivity of SCMO is a good evidence that the oxygen vacancy level is low enough to present quite limited effects on the whole picture of transport behavior. On the other hand, the oxygen vacancy level can tune the STO to conducting. Thus, a control set of the sample S_0 was employed during the fabrication of S_5, in which we set a mask between the substrate and target. As shown in Supplementary Fig. S10, the pure STO substrate treated with high temperature at high vacuum (same conditions as S_5) exhibits resistivity of ~2 kΩ magnitude, and neglectable MR.

Since the high uniformity of the SCMO thin films is verified by XRD and HRTEM, the model of heavily disordered semiconductors[4,31] is not suitable for this case. The high carriers' concentration of SCMO thin films, as well as the DFT calculations, suggests that the Fermi pockets are too large for 14 T field to quantize carriers into zeroth Landau Level, therefore the quantum MR model is not applicable for SCMO either[32]. LMR also been reported in 2D electron gas system, which originates from the giant Hall effect contributing to longitudinal MR due to the carrier density fluctuation[33]. However, in SCMO, the Hall effect is weaker than longitudinal MR, which means the carrier density fluctuation induced Hall effect component only have limited contribution to MR behavior. Note that the LMR effect in ferromagnetic SrRuO$_3$ thin films are dominated by linear dispersed Weyl bands, similar to other topological materials[13]. Therefore, it is reasonable to deduce that the LMR behavior in SCMO is similar to the topological insulators TlBiSeS[8] or Dirac semimetals Cd$_3$As$_2$:[11,12] GC motion dominant behavior. In Cd$_3$As$_2$ single crystal, LMR arises because the local current density acquires spatial fluctuations in both magnitude and direction, as a result of the heterogeneity or microstructure caused by nonhomogeneous carrier and mobility distribution. The GC motion is perpendicular to cycloid motion in the magnetic fields, due to the effects of the electric field. During GC motion across low-mobility islands, multiple small-angle scattering occurs and thus the LMR effect can be observed. In this model, the conductor should be in three dimensional to allow electrons moving in z direction. There's a crossover effect within this model, which is, the resistivity increases parabolically with field in low-field regime (below the critical value: B_L), and LMR is only observed when magnetic field is sufficiently large ($B \gg B_L$)[11,14].

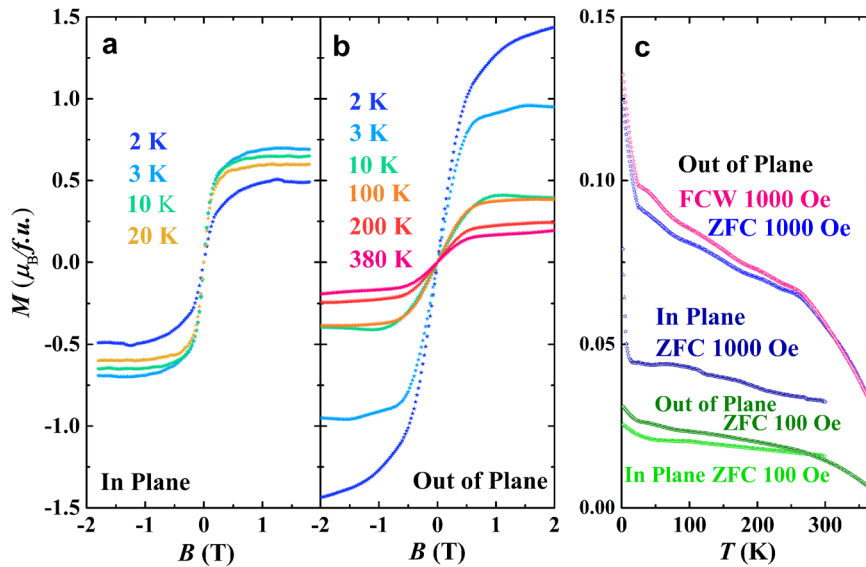**Fig. 4 Magnetic properties of SCMO thin film S_5. a, b** The magnetic hysteresis curves of SCMO at various temperatures. **c** The temperature-dependent magnetization curves range from 2 K to 300 K, with 100 Oe and 1000 Oe applied field in ZFC and FC process, respectively.

We thus carefully conducted low-field MR measurements with small steps on S_5 below 10 K, as shown in Fig. 2d. One may notice that, in low-field region, the MR curves increase quasi-parabolically with the magnetic field to B_L, and further increase linearly, which exactly fits to the GC motion model. In the GC model explained by Song et al.[14] a feature of GC motion governed LMR is that the MR can be described in Kohler's rule since it scales with mobility. We employ Kohler's plot here at high magnetic field regime (Fig. 2e) and low-field regime (Fig. 2f), with different scaling rule, e.g., due to the Hall angle difference (Supplementary Fig. S12), Fig. 2e is scaled with resistivity, mobility, and Hall angle, whereas Fig. 2f is directly scaled with resistivity. In low-field and high field limit, the data coincide with each other quite well, which suggests the different scattering mechanisms above and below B_L. The crossover effect is a signature of GC motion dominant MR behavior, which can be found in all LMR curves in SCMO.

The similar linear or quasi-linear MR can be found in S_1–S_7 series SCMO samples, including the thin-limit (6 nm) sample, as shown in Supplementary figs. S3–S9. Since the thin films crystallize in a cubic lattice with a normal vector of (001), there should be less anisotropy intrinsically within- and out-of-thin film plane. It is obvious that the MR originates from Lorenz force, which results in greater MR for magnetic field-perpendicular-to-current configurations (T and V). Moreover, the thin film shape favors cyclotron orbits with angular moment parallel to the normal vector, meanwhile the perpendicular orbits suffer more from surface scattering. The abovementioned effect could be more obvious in thin-limit samples, e.g., in S1–S3, the 2 K and 14 T T- and V-MR values are at least twice larger than P-MR value.

Magnetic properties

Since the ground state of SCMO is half-metallic, the carriers are fully spin-polarized, and effectively scattered by the magnetic domain structure, the magnetic properties are important to the LMR effect. To directly test this, we conducted the temperature and magnetic field dependent magnetization measurements of SCMO thin film S5 . We measured the hysteresis loops at various temperatures from 3 K to 380 K within and perpendicular to the thin film plane, which are shown in Fig. 4a, b. Please notice that the moment is obtained via subtracting a linear diamagnetic component contributed by STO substrate. The moment was converted from the total magnetization to Bohr magneton per

formula unit. The in-plane saturation moment at 2 K is ~0.5 μ_B/f.u., which slightly increases to ~0.7 μ_B/f.u. at 3 K, and then decreases to ~0.65 μ_B/f.u. at 10 K, and 0.6 μ_B/f.u. at 20 K. With the magnetic field perpendicular to the film plane, the saturation moment is ~1.45 μ_B/f.u. at 2 K, and decreases to ~0.25 μ_B/f.u. at 380 K. This is, however, less than expected for a fully aligned Cr^{3+} (3 μ_B) and Mo^{5+} (1 μ_B), which would be ~2 μB for an antiferromagnetic collinearly-aligned Cr^{3+}-Mo^{5+} spin dimer. One may note that, the saturation moment changes with temperature drastically in 2–380 K regime, which is unusual in a ferrimagnet ordered at high temperatures (above 400 K). To solve this question, direct measurement of the magnetic moment via neutron scattering or X-ray magnetic circular dichroism is desired. Further, we measured the temperature-dependent magnetization curves in both zero-field-cooling (ZFC) and field-cooling with data collected on warming (FCW) procedures between 3 and 380 K. After subtracting the temperature-dependent diamagnetic background obtained from MH loop subtraction, the temperature-dependent magnetic moments of pure SCMO thin film are shown in the Fig. 4c, with 100 and 1000 Oe applied magnetic field. One can see the clear difference of the ZFC & FCW curves in the 1000 Oe out-of-plane curves, indicating a slight history-dependence of the magnetization, which is a hallmark of a magnetically ordered state. Similar behaviors can be found in other measurements, however, only ZFC curves are present to make the graph clear enough to read. The ferrimagnetic transition temperature T_C of SCMO is ~450 K[34], which indicates all the transport and magnetic measurements are in ferrimagnetic ordering regime. We note that the domain structures of ferro-/ferri-magnetic thin films observed at low temperatures are well studied, e.g., yttrium iron garnet (YIG) films show long tail stripes domain structure below T_C, which is still clear at low temperatures[35]. Therefore, we believe that the domain structure exists in SCMO thin films at low temperature, and contributes to the carrier scattering process. One interesting point is, the MT curves show upturn below ~20 K, which indicates the larger moment of SCMO, together with the high mobility and large MR values. In the high mobility regime, $\omega_c \gg 1$ and carriers' trajectories are dominated by GC motions. During the GC drifts from one magnetic domain to another, the spin–spin interaction may occur at the domain wall, which scatters the carriers. Thus, the GC motion would undergo backscattering or small-angle grazing near the domain wall, similar to the GC motion picture through mobility fluctuation area in Cd_3As_2[11,14]. It should be noted
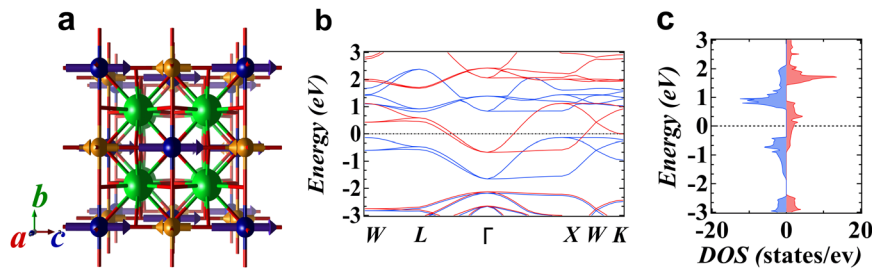
Fig. 5 Structure, electronic band structure, and density of states of the double perovskite Sr$_2$CrMoO$_6$. a Face-centered cubic structure of the double perovskite Sr$_2$CrMoO$_6$. **b** Electronic band structure taken on a selected path through the Brillouin zone. **c** Spin-resolved density of states integrated over the entire Brillouin zone showing spin-up states at the Fermi level with 100% spin polarization.

that the LMR effect of metallic ferromagnetic system has been observed in Cr/Ag/Cr sandwich structure[36] and LaMn$_2$Ge$_2$ poly-crystals[37]. The LMR effect in SCMO would be an intrinsic property to half-metallic/ferromagnetic-metallic systems, which broadens the LMR research, as well as its application in more material systems.

Theoretical calculations

To verify that the observed magnetic properties are consistent with the half-metallic double perovskite phase, ab initio calculations were performed. Figure 5a shows the idealized crystals structure after atomic relaxation with perfect superlattice formed by alternating Mo/Cr sites. The direction and magnitude of the magnetic moments are shown by the vectors in the structure. The magnetic moments in this configuration were found to arrange in a simple G-type ferrimagnetic ground state with Cr (2.24 μ_B) and Mo (0.43 μ_B) giving a net moment of 1.86 μ_B in reasonable agreement with experiment. The small mismatch between the experimental data and theory may be attributed to the role of a small number of anti-site defects (where Cr and Mo mix on their various sites) which can reduce the net moment in a ferrimagnet double perovskite[38,39]. The anti-site defects could also lead to disorder-induced positive MR, and therefore contribute to total magnetotransport behavior. Figure 5b, c show the corresponding band-structure and spin-polarized density of states respectively. One of the spin-states is gapped, whereas the other shows states at the Fermi level – a characteristic of a half-metal. Examination of the projected density of states reveals that the states near the Fermi level are almost entirely formed by Mo-3d states, and the splitting thereof is therefore caused by the onsite exchange interaction. Calculations including the spin–orbit interaction show that this well-defined splitting between the spin-states is preserved, as expected given the relatively weak atomic spin–orbit interaction of Mo and thus the half metallicity is robust. The unusual band structure gives rise to an electron parabolic band at Γ that coexists with a hole band at W. The latter band has a linear dispersion, and identical Dirac-line feature is observed in the exchange split band for spin-down states below the Fermi level. The Dirac-feature bands may contribute to the high mobility of SCMO, which ensures cyclotron motion dominating magnetotransport behavior at experimentally achieved magnetic fields. This is an important point of observing LMR effect in SCMO thin films.

In summary, various SCMO thin films with different thicknesses were deposited on STO single-crystal substrates. The crystallization quality is excellent, which is evidenced by XRD and HRTEM. DFT calculations suggest that the cubic double perovskite SCMO is a half metal, with intrinsically antiparallel coupled Cr^{3+} and Mo^{3+} moments, which agrees well with the magnetization measurements. Magnetization measurements of SCMO thin films presented nearly-neglectable-coercivity MH curves, with out-of-plane saturation moments of ~1.45 μ_B/f.u. at 2 K, which is close to the DFT calculated 1.86 μ_B/f.u. with ferrimagnetic coupling. SCMO possesses nΩ·cm magnitude resistivity and ultrahigh mobility (10^4 cm^2 V^{-1} s^{-1}) in all half metals, which provides a platform for

low-dispassion fully spin-polarized current. In cryogenic temperatures, SCMO exhibits LMR behavior, which is probably contributed by the GC motion across magnetic domain. Our DFT calculations further show Dirac-like bands near the Fermi level, which could be a good reason of the high mobility in SCMO. The unusual behavior in SCMO expands giant positive linear magnetoresistance research in oxide materials, which will attract more fundamental and application research in double perovskite systems.

METHODS

Preparation of Sr$_2$CrMoO$_6$ ceramic target

A ceramic target with nominal composition of Sr$_2$CrMoO$_6$ was prepared by the conventional solid-state reaction method using stoichiometric Sr (SrCO$_3$ (99.95%)), Cr (Cr$_2$O$_3$(99.95%)), and Mo (MoO$_3$ (99.95%)) as starting materials. The starting materials are well mixed via ball milling for 20 h and sintered at 950 °C for 12 h to complete the chemical reaction. The obtained polycrystal sample was further grounded into a fine powder via 20 h ball milling, and cold-pressed into a pellet. The pellet was sintered at 1100 °C for 12 h to obtain the ceramic target with a diameter of 25 mm.

Thin film growth

Pulsed laser deposition (PLD) apparatus equipped with a KrF ($\lambda = 248$ nm) excimer laser was employed to grow Sr$_2$CrMoO$_6$ (SCMO) thin films on one-side polished (001)-oriented SrTiO$_3$ (STO) single-crystal substrates. Since the target and thin film are in different chemical composition, the high-vacuum condition is necessary to guarantee low-oxygen thin film deposition. Before deposition, the chamber has been pumped into high vacuum with a pressure of 5.0×10^{-5} Pa. The deposition process has been carried out at 5.0×10^{-5} Pa for 2.5–90 min for different samples with a substrate temperature of 775 °C, followed by in-situ annealing for 30 min. Then the film has been cooled down to room temperature at a rate of 10 °C min^{-1}. The distance between the target and the substrate was set as 5 cm. The laser energy density and repetition rate are 1 J/cm^2 and 2 Hz, respectively. The film thickness is controlled by the number of laser pulses.

Structural characterization

The structural crystallization of SCMO thin film has been characterized via X-ray diffraction (XRD) rocking curve, θ–2θ and φ-scans, and reciprocal space mapping using an x-ray diffractometer (PANalytical X'Pert MRD) equipped with Cu $K\alpha_1$ radiation ($\lambda = 1.5406$ Å). Cross-section microscopic structural properties have been characterized via high-resolution transmission electron microscopy (HRTEM) images and selected area electron diffraction (SAED) using a Tecnai G2F20 S-Twin transmission electron microscope. Sample for HRTEM measurements was cut into lamellas by Focused Ion Beam (Scios 2 HiVac, Thermo Fisher).

Electronic transport measurements

Ohmic contacts were employed on the silver-patterned thin film surface with four-parallel electrodes configurations to conduct the magnetotransport measurements up to 14 T in a physical property measurement system (PPMS-14, Quantum Design). Hall measurements were performed via the Van de Pauw configuration using PPMS. The magnetic properties are measured using the SQUID magnetometer up to 7 T (MPMS3, Quantum Design).

Computational calculation methods

Electronic structure calculations were performed using density functional theory (DFT) in the Vienna Ab Initio Simulation Package (VASP)[40–42]. The exchange-correlation energy was described using the generalized-gradient approximation described by Perdew et al. (GGA-PBE)[43]. The projector augmented-wave method was used to represent the ionic cores[40–42], and the number of valence electrons in the atomic electronic state of Sr, Cr, Mo, and O were 10, 12, 14, and 6 respectively. Wave functions were presented in a plane-wave basis and the cut-off energy was 500 eV. Structural data taken from Parish et al.[4] (ref. [44]) was used as the input, and initially, the system was assumed to exhibit perfect structural order on the Cr/Mo sites to give an ideal double perovskite in the $F_{m\bar{3}m}$ space group. Ionic and cell relaxation was performed until the forces converged to beneath 0.01 eV/Å. A gamma-centered $8 \times 8 \times 8$ k-mesh was used for the density of states calculation, and the eigenvalues were calculated along a standard k-path through the Brillouin zone for the band structure calculations.

DATA AVAILABILITY

The authors declare that the data supporting the findings of this study are available within the article and its Supplementary Information files.

REFERENCES

1. Ali, M. N. et al. Large, non-saturating magnetoresistance in WTe₂. *Nature* **514**, 205–208 (2014).
2. Wang, K., Graf, D., Li, L., Wang, L. & Petrovic, C. Anisotropic giant magnetoresistance in NbSb₂. *Sci. Rep.* **4**, 7328 (2014).
3. Guo, L. et al. Extreme magnetoresistance and SdH oscillation in compensated semimetals of NbSb₂ single crystals. *J. Appl. Phys.* **123**, 155103 (2018).
4. Parish, M. M. & Littlewood, P. B. Non-saturating magnetoresistance in heavily disordered semiconductors. *Nature* **426**, 162–165 (2003).
5. Xu, R. et al. Large magnetoresistance in non-magnetic silver chalcogenides. *Nature* **390**, 57–60 (1997).
6. Lee, M., Rosenbaum, T. F., Saboungi, M.-L. & Schnyders, H. S. Band-gap tuning and linear magnetoresistance in the silver chalcogenides. *Phys. Rev. Lett.* **88**, 066602 (2002).
7. Wang, X., Du, Y., Dou, S. & Zhang, C. Room temperature giant and linear magnetoresistance in topological insulator Bi₂Te₃ nanosheets. *Phys. Rev. Lett.* **108**, 266806 (2012).
8. Novak et al. Large linear magnetoresistance in the Dirac semimetal TlBiSSe. *Phys. Rev. B* **91**, 041203 (2015).
9. Huang, X. et al. Observation of the chiral-anomaly-induced negative magnetoresistance in 3D Weyl semimetal TaAs. *Phys. Rev. X* **5**, 031023 (2015).
10. Xiong, J. et al. Anomalous conductivity tensor in the Dirac semimetal Na₃Bi. *EPL* **114**, 27002 (2016).
11. Narayanan, A. et al. Linear magnetoresistance caused by mobility fluctuations in n-doped Cd₃As₂. *Phys. Rev. Lett.* **114**, 117201 (2015).
12. Feng, J. et al. Large linear magnetoresistance in Dirac semimetal Cd₃As₂ with Fermi surfaces close to the Dirac points. *Phys. Rev. B* **92**, 081306 (2015).
13. Takiguchi, K. et al. Quantum transport evidence of Weyl fermions in an epitaxial ferromagnetic oxide. *Nat. Commun.* **11**, 1–12 (2020).
14. Song, J. C. W., Refael, G. & Lee, P. A. Linear magnetoresistance in metals: guiding center diffusion in a smooth random potential. *Phys. Rev. B* **92**, 180204 (2015).
15. Lee, S. et al. Electrically driven phase transition in magnetite nanostructures. *Nat. Mater.* **7**, 130–133 (2008).
16. Shimakawa, Y. et al. Crystal structure, magnetic and transport properties, and electronic band structure of A₂Mn₂O₇ pyrochlores, (A=Y, In, Lu and Tl). *Phys. Rev. B* **59**, 1249–1254 (1999).
17. Hwang, H. Y., Cheong, S. W., Ong, N. P. & Batlogg, B. Spin-polarized Intergrain tunneling in La₂/₃Sr₁/₃MnO₃. *Phys. Rev. Lett.* **77**, 2041–2044 (1996).
18. García-Hernández, M., Martínez, J. L., Martínez-Lope, M. J., Casais, M. T. & Alonso, J. A. Finding universal correlations between cationic disorder and low field magnetoresistance in FeMo double perovskite series. *Phys. Rev. Lett.* **86**, 2443 (2001).
19. Kobayashi, K. I., Kimura, T., Sawada, H., Terakura, K. & Tokura, Y. Room-temperature magnetoresistance in an oxide material with an ordered double-perovskite structure. *Nature* **395**, 677–680 (1998).
20. Kato, H. et al. Metallic ordered double-perovskite Sr₂CrReO₆ with maximal Curie temperature of 635 K. *Appl. Phys. Lett.* **81**, 328–330 (2002).
21. Philipp, J. B. et al. Structural and doping effects in the half-metallic double perovskite A₂CrWO₆. *Phys. Rev. B* **68**, 399–404 (2003).
22. Pardo, V. & Pickett, W. E. Compensated magnetism by design in double perovskite oxides. *Phys. Rev. B* **80**, 054415 (2009).
23. Tomioka, Y. et al. Magnetic and electronic properties of a single crystal of ordered double perovskite Sr₂FeMoO₆. *Phys. Rev. B* **61**, 422–434 (2000).
24. Kobayashi, K. I. et al. Intergrain tunneling magnetoresistance in polycrystals of the ordered double perovskite Sr₂FeReO₆. *Phys. Rev. B* **59**, 11159 (1999).
25. Zhang, J. et al. Giant positive magnetoresistance in half-metallic double-perovskite Sr₂CrWO₆ thin films. *Sci. Adv.* **3**, e1701473 (2017).
26. Tian, T. et al. Ultrahigh mobility and giant magnetoresistance in the Dirac semimetal Cd₃As₂. *Nat. Mater.* **14**, 280–284 (2015).
27. Guo, L. et al. Electronic transport evidence for topological nodal-line semimetals of ZrGeSe single crystals. *ACS Appl. Electron. Mater.* **1**, 869–876 (2019).
28. Singha, R., Pariari, A. K., Satpati, B. & Mandal, P. Large nonsaturating magnetoresistance and signature of nondegenerate Dirac nodes in ZrSiS. *Proc. Natl Acad. Sci. USA* **114**, 2468–2473 (2017).
29. Tafti, F. F., Gibson, Q. D., Kushwaha, S. K., Haldolaarachchige, N. & Cava, R. J. Resistivity plateau and extreme magnetoresistance in LaSb. *Nat. Phys.* **12**, 272–277 (2016).
30. Jo, N. H. et al. Extremely large magnetoresistance and Kohler's rule in PdSn₄: a complete study of thermodynamic, transport, and band-structure properties. *Phys. Rev. B* **96**, 165145 (2017).
31. Jingshi, H. U. & Rosenbaum, T. F. Classical and quantum routes to linear magnetoresistance. *Nat. Mater.* **7**, 697–700 (2008).
32. Abrikosov, A. A. Quantum magnetoresistance. *Phys. Rev. B* **58**, 2788–2794 (1998).
33. Khouri, T. et al. Linear magnetoresistance in a quasifree two-dimensional electron gas in an ultrahigh mobility GaAs quantum well. *Phys. Rev. Lett.* **117**, 256601 (2016).
34. Arulraj, A., Ramesha, K., Gopalakrishnan, J. & Rao, C. N. R. Magnetoresistance in the double perovskite Sr₂CrMoO₆. *J. Solid State Chem.* **155**, 233–237 (2000).
35. Wang, R., Shang, Y. X., Wu, R., Yang, J. B. & Ji, Y. Evolution of magnetic domain structure in a YIG thin film. *Chin. Phys. Lett.* **33**, 126–129 (2016).
36. Verbanck, G. et al. Large positive magnetoresistance in Cr/Ag/Cr trilayers. *Appl. Phys. Lett.* **70**, 1477–1479 (1997).
37. Mallik, R., Sampathkumaran, E. V. & Paulose, P. L. Large positive magnetoresistance at low temperatures in a ferromagnetic natural multilayer, LaMn₂Ge₂. *Appl. Phys. Lett.* **71**, 2385–2387 (1997).
38. Bertinshaw, J. et al. Spin-cycloid instability as the origin of weak ferromagnetism in the disordered perovskite Bi₀.₈La₀.₂Fe₀.₅Mn₀.₅O₃. *Phys. Rev. B* **89**, 144422 (2014).
39. McBride, B. R. et al. Study of the B-site ion behaviour in the multiferroic perovskite bismuth iron chromium oxide. *J. Appl. Phys.* **123**, 154104 (2018).
40. Kresse, G. G. & Furthmüller, J. J. Efficient iterative schemes for ab initio total-energy calculations using a plane-wave basis set. *Phys. Rev. B* **54**, 11169–11186 (1996).
41. Kresse, G. & Furthmüller, J. Efficiency of ab-initio total energy calculations for metals and semiconductors using a plane-wave basis set. *Comput. Mater. sci.* **6**, 15–50 (1996).
42. Kresse, G. & Hafner, J. Ab initio molecular dynamics for liquid metals. *Phys. Rev. B* **47**, 558 (1993).
43. Perdew, J. P., Burke, K. & Ernzerhof, M. Generalized gradient approximation made simple. *Phys. Rev. lett.* **77**, 3865–3868 (1996).
44. Blasco, J., Ritter, C., Rodríguez-Velamazán, J. A. & Herrero-Martín, J. Electron doping versus antisite defects: Structural and magnetic properties of Sr₂₋ₓLaₓCrMoO₆ and Sr₂₋ₓLaₓCr₁₊ₓ/₂Mo₁₋ₓ/₂O₆ perovskites. *Solid State Sci.* **12**, 750–758 (2010).

ACKNOWLEDGEMENTS

AUTHOR CONTRIBUTIONS

R.K.Z. and W.Z. conceived the idea and supervised the research. Z.C.W. prepared thin films. Z.C.W. and S.S.L conducted electronic transport and AFM measurements. L.C. contributed to the data analyses. G.Y.G. and J.S.Y. performed XRD and TEM measurements. F.T. and Y.F. conducted magnetic measurements. D.C. performed DFT calculations and analyzed computational data. X.W. contributed to the discussion of the results. Z.C.W., W.Z., and R.K.Z. wrote the manuscript. All authors contributed to the discussion of the results and the revision of the manuscript.

COMPETING INTERESTS

The authors declare no competing interests.

ADDITIONAL INFORMATION

Supplementary information The online version contains supplementary material available at https://doi.org/10.1038/s41535-021-00354-1.

Correspondence and requests for materials should be addressed to W.Z. or R.-K.Z.

Reprints and permission information is available at http://www.nature.com/reprints

Publisher's note Springer Nature remains neutral with regard to jurisdictional claims in published maps and institutional affiliations.